

# Regular chains of star formation complexes in spiral arms of NGC 628

A. S. Gusev and Yu. N. Efremov

*Sternberg Astronomical Institute, Lomonosov Moscow State University, Universitetsky pr. 13, 119992 Moscow, Russia, gusev@sai.msu.ru*

Accepted 2013 June 6. Received 2013 June 6; in original form 2013 January 26

## ABSTRACT

We investigate photometric properties of spiral arms and stellar complexes/associations inside these arms in the grand design NGC 628 (M 74) galaxy. We analyze *GALEX* ultraviolet, optical *UBVRI*, and  $H\alpha$  surface photometry data, including those obtained with 1.5 m telescope at the Maidanak Observatory. In the longer arm, the large and bright stellar complexes are located at regular intervals along the arm, but only farther from the galaxy center. They are joined with the narrow lane of dust, visible only in the infrared bands. The usual dust lane along the stellar arm inner side is seen there only at distances closer to the galaxy center. It is well expressed in CO ( $H_2$ ) image. We have found, that the second, short arm hosts two dust lanes, the strong and wide at the inner side, and narrow and irregular along its outer edge. This outer dust lane is well seen in IR images only. The shorter arm contains no star complexes at all. Gradients of age and luminosity of stars across both arms are missing (again excepting the parts of arms located closer to the center), which is confirmed by our photometric cuts across both arms. The drastic difference in the morphology of the two symmetric arms (grand design type) of a galaxy has now been confirmed by objective measurements in the case of M 74. It is unclear why about two third of galaxies with beaded arms host these "beads" (star complexes) in one arm only.

**Key words:** galaxies: structure – galaxies: individual: NGC 628 (M 74) – H II regions – ultraviolet: galaxies

## 1 INTRODUCTION

The young stars and clusters, as well as H II regions are known to be distributed along the spiral arms of grand design galaxies non-uniformly; rather often they form groupings with sizes of about 0.3–0.7 kpc, rarely a little more. Older objects (such as Cepheids, most of which are ten times older than O stars) are usually also gathered in the same groups, called star complexes (Efremov 1979). These complexes are the greatest coherent groupings of stars and clusters, which are connected by unity of an origin from the same  $H\text{I}/H_2$  supercloud (Efremov 1989, 1995; Elmegreen 1994, 2009; Odekon 2008; de la Fuente Marcos & de la Fuente Marcos 2009).

In irregular galaxies, there is a continuous sequence of star groupings with increasing age (of the oldest stars) and size, starting from clusters to associations to complexes (Efremov & Elmegreen 1998); in flocculent galaxies the largest complexes transform to short spiral segments (Elmegreen & Efremov 1996). Within the regular spiral arms of grand design galaxies, star complexes sometimes are located along an arm at rather regular distances. This is a quite rare phenomenon, which was found by Elmegreen & Elmegreen (1983) in 22 galaxies. They noted the spacing of complexes (which they called H II regions) in studied galaxies to be within 1–4 kpc, and each string to consist, on aver-

age, of five H II regions. The gravitational or magneto-gravitational instability developing along the arm was suggested to explain this regularity (Elmegreen & Elmegreen 1983; Elmegreen 1994).

The list of Elmegreen & Elmegreen (1983) is still the only published result of systematic searches for string of complexes in spiral arms. Note that in 15 of their 22 galaxies the regular strings of complexes are seen in one arm only. We believe, to study properties of such galaxies is a most perspective way to understand the nature of regular chains formation.

One of such galaxies is M 31, as it is seen in the *GALEX* UV images. Efremov (2009, 2010) noticed a regular string of star complexes there, located in the north-western arm; it has about the same size – 0.6 kpc with spacing of 1.1 kpc. Within the same arm segment, a regular magnetic field with a wavelength of 2.3 kpc was found earlier by Beck et al. (1989). This wavelength is twice as large as the spacing between complexes and suggests that they were formed as a result of the magneto-gravitational instability developed along the arm. In this north-western arm segment, star complexes are located inside the gas-dust lane, whilst in the south-western arm of M 31 the gas-dust lane is upstream of the bright and uniform stellar arm. Earlier, evidence for the age gradient was found in the south-western arm. All these are signatures of a spiral shock, which may be associated with an unusually large (for

arXiv:1306.1731v1 [astro-ph.CO] 7 Jun 2013

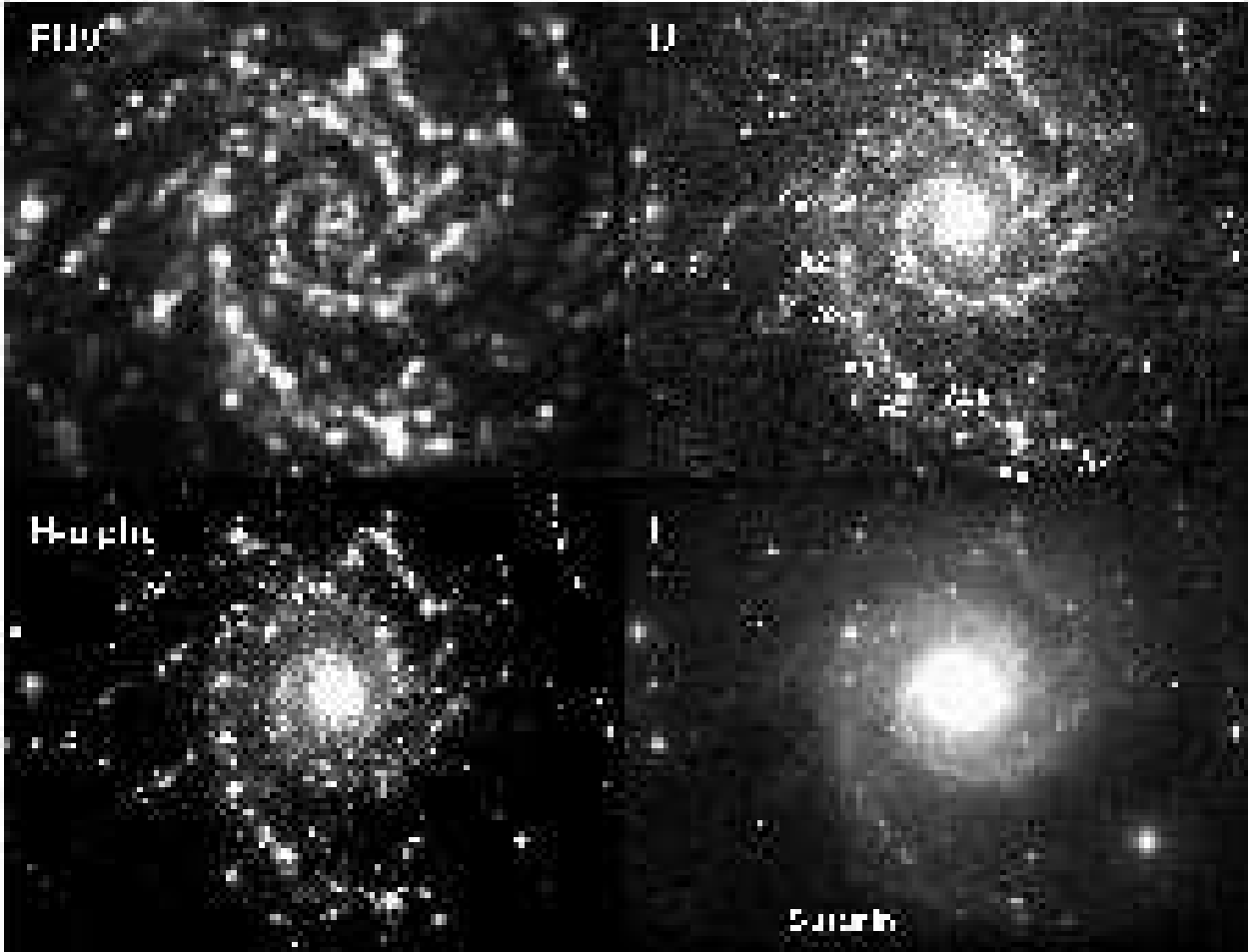


**Figure 1.** Images of NGC 628 in the *FUV* (top-left), *U* (top-right), *I* (bottom-right) passbands, and  $H\alpha$  line (bottom-left). The *FUV* image was taken from *GALEX* archive, the *U*, *I* and  $H\alpha$  images were obtained on the Maidanak Observatory with the 1.5 m telescope. Positions and ID numbers of star formation complexes from the list of Elmegreen & Elmegreen (1983) are indicated in the *U* image. North is upward and east is to the left. **High resolution jpeg image is available in the source format.**

**Table 1.** Basic parameters of NGC 628.

Parameter	Value
Type	Sc
Total apparent <i>B</i> magnitude ( $B_t$ )	9.70 mag
Absolute <i>B</i> magnitude ( $M_B$ ) <sup>a</sup>	-20.72 mag
Inclination ( <i>i</i> )	7°
Position angle (P.A.)	25°
Heliocentric radial velocity ( <i>v</i> )	659 km/s
Apparent corrected radius ( $R_{25}$ ) <sup>b</sup>	5.23 arcmin
Apparent corrected radius ( $R_{25}$ ) <sup>b</sup>	10.96 kpc
Distance ( <i>d</i> )	7.2 Mpc
Galactic absorption ( $A(B)_{Gal}$ )	0.30 mag
Distance modulus ( $m - M$ )	29.29 mag

<sup>a</sup> Absolute magnitude of a galaxy corrected for Galactic extinction and inclination effect.

<sup>b</sup> Isophotal radius (25 mag arcsec<sup>-2</sup> in the *B*-band) corrected for Galactic extinction and absorption due to the inclination of NGC 628.

M 31) pitch angle of this south-western arm segment. Such a shock may prevent the formation of a regular magnetic field, which might explain the absence of star complexes there. The fragmentation of

the outer  $H\text{I}$  arms of our Galaxy into regularly spaced superclouds was also described (Efremov 2011); a magnetic field parallel to the Galactic planes is known there but no details are available yet.

Anticorrelation between shock wave signatures and the presence of star complexes is observed in spiral arms of a few other galaxies. Regular chains of star complexes/superclouds in spiral arms are rare, which may imply that a specific mechanism is involved in their formation; the most probable is the Parker-Jeans instability. Unfortunately, there are no sufficiently detailed magnetic field data (or no such data at all) to compare them with the arm structures.

Amongst nearby galaxies, the most evident (after M 31) case of the above-mentioned anticorrelation is NGC 628 (M 74) galaxy. It is a nearby spiral galaxy viewed almost face-on (Fig. 1). It is also an excellent example of a galaxy with regular strings of complexes which are seen in one arm only. It hosts two regular arms, the longer one of which includes a number of star complexes with similar spacing. In this longer arm Elmegreen & Elmegreen (1983) found seven bright complexes ( $H\text{II}$  regions) plus a fainter one with a characteristic separation of 1.6-1.7 kpc (Fig. 1). Another arm does not contain evident complexes, but instead the strong dust lane is seen along the arm inner side (and the fainter one along the outer side).

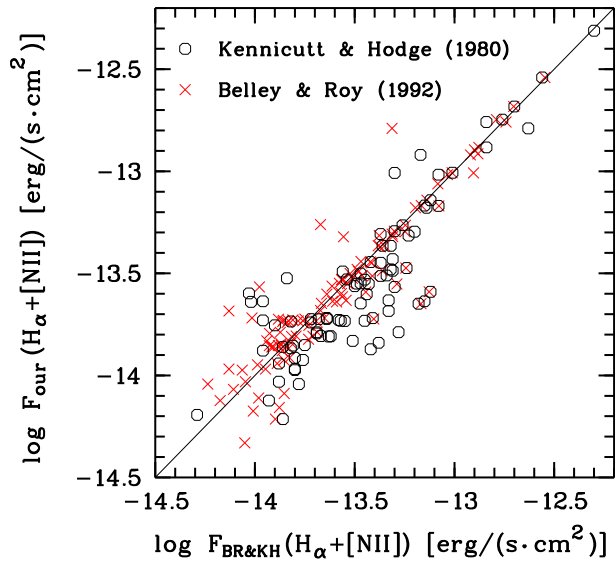


**Figure 2.** Comparison between our data (ordinate axis) and data of Belley & Roy (1992); Kennicutt & Hodge (1980) (abscissa axis) of spectrophotometric  $H\alpha$ + $[NII]$  fluxes for  $HII$  regions in NGC 628.

Here, we consider a regularity of distribution in spacing and photometric properties of star formation regions (SFRs) in well-known grand design galaxy NGC 628, based on our own observations in the  $U$ ,  $B$ ,  $V$ ,  $R$ ,  $I$  passbands, and  $H\alpha$  line, as well as *GALEX* far- and near-ultraviolet (*FUV* and *NUV*) data. We use the term “star formation regions”, which includes young star complexes, young clusters, OB-associations,  $HII$  regions, i.e. all young stellar groups independently from their sizes and luminosities.

The fundamental parameters of NGC 628 are presented in Table 1. We take the distance to NGC 628, obtained in Sharina, Karachentsev & Tikhonov (1996); van Dyk, Li & Filippenko (2006). We used the position angle and the inclination of the galactic disk, derived by Sakhibov & Smirnov (2004), based on a Fourier analysis of the spatial distribution of the radial velocities of the gas in the disk. Other parameters were taken from the LEDA data base<sup>1</sup> (Paturel et al. 2003). We adopt the Hubble constant  $H_0 = 75 \text{ km s}^{-1}\text{Mpc}^{-1}$  in the paper. With the assumed distance to NGC 628, we estimate a linear scale of 34.9 pc/arcsec.

## 2 OBSERVATIONS AND REDUCTION

The results of *UBVRI* photometry for NGC 628 have already been published in Bruevich et al. (2007). Here we present  $H\alpha$  spectrophotometric observations and data reduction for the galaxy, that have not been published earlier. Just a brief compilation is given for our older observations, as well as for *GALEX* ultraviolet data.

### 2.1 Observations

The photometric observations were obtained in September 2002 with the 1.5 m telescope of the Maidanak Observatory (Institute of Astronomy of the Academy of Sciences of Uzbekistan) using a

SITe-2000 CCD array. The focal length of the telescope is 12 m. Detailed description of the telescope and the CCD camera can be found in Artamonov et al. (2010). With broadband  $U$ ,  $B$ ,  $V$ ,  $R$ , and  $I$  filters, the CCD array realizes a photometric system close to the standard Johnson–Cousins *UBVRI* system. The camera is cooled with liquid nitrogen. The size of the array is  $2000 \times 800$  pixels. It provides the  $8.9 \times 3.6 \text{ arcmin}^2$  field of view with the image scale of 0.267 arcsec/pixel. The seeing during the observations was 0.7–1.1 arcsec.

Since angular size of NGC 628 was larger than the field of view, we obtained separate images for the northern and southern parts of the galaxy.

Spectrophotometric  $H\alpha$  observations of NGC 628 were made on 2006 September 26 with the 1.5-m telescope of the Mt. Maidanak Observatory with the SI-4000 CCD camera. The chip size,  $4096 \times 4096$  pixels, provides a field of view of  $18.1 \times 18.1 \text{ arcmin}^2$ , with an image scale of 0.267 arcsec/pixel. The total exposure time was 1200 s, the seeing was 1.0 arcsec.

The wide-band interference  $H\alpha$  filter ( $\lambda_{eff} = 6569\text{\AA}$ , FWHM =  $44\text{\AA}$ ) was used for the observations. Indicated filter parameters provides  $H\alpha$ + $[NII]\lambda 6548+\lambda 6584$  imaging for nearby galaxy NGC 628.

Ultraviolet *GALEX FUV* and *NUV* reduced FITS-images of NGC 628 were downloaded from Barbara A. Miculski archive for space telescopes (galex.stsci.edu; source G13\_050001\_NGC628). The observations were made in October–November 2007. The total exposure time was 12004.6 s for every band. The description of the *Galaxy Evolution Explorer* mission and basic parameters of passbands were presented in Morrissey et al. (2005). We only note here, that an effective wavelength  $\lambda_{eff} = 1528\text{\AA}$  for the *FUV* band and  $2271\text{\AA}$  for the *NUV* band, and image resolution is equal to 4.5 arcsec for *FUV* and 6.0 arcsec for *NUV*.

### 2.2 Data reduction

The reduction of the photometric and spectrophotometric data was carried out using standard techniques, with the European Southern Observatory Munich Image Data Analysis System<sup>2</sup> (*ESO-MIDAS*) (Banse et al. 1983; Grøsbol & Ponz 1990). The main image reduction stages for spectrophotometric data were as follows: correction for bias and flat field; removal of cosmic-ray traces; determining the sky background, then subtracting it from each image frame; aligning and adding the images; absolute calibration. The main photometric *UBVRI* image reduction stages were described in detail in Bruevich et al. (2007).

Calibration of  $H\alpha$  fluxes the was made based on the results of spectrophotometric observations of Belley & Roy (1992); Kennicutt & Hodge (1980). We calculated fluxes of  $HII$  regions using our images with apertures of Belley & Roy (1992); Kennicutt & Hodge (1980) and found coefficient of reduction from our instrumental  $H\alpha$  flux to the flux in physical units ( $\text{erg s}^{-1} \text{cm}^{-2}$ ):

$$F = (3.70 \pm 0.60) \times 10^{-18} \text{ erg s}^{-1} \text{ cm}^{-2} / \text{ADU}$$

by data of Belley & Roy (1992), and

$$F = (4.48 \pm 1.48) \times 10^{-18} \text{ erg s}^{-1} \text{ cm}^{-2} / \text{ADU}$$

by data of Kennicutt & Hodge (1980). The value  $3.70 \times 10^{-18}$  for the reduction coefficient was adopted.

Fig. 2 compares  $H\alpha$ + $[NII]$  fluxes derived in the present

<sup>1</sup> <http://leda.univ-lyon1.fr/>

<sup>2</sup> <http://www.eso.org/sci/software/esomidas/>

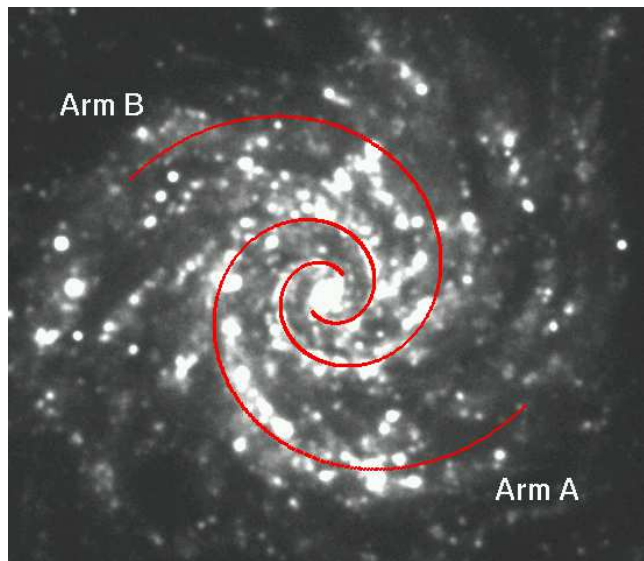


**Figure 3.** *NUV* image of NGC 628 with overlaid logarithmic spirals. The size of the image is  $9.7 \times 8.5$  arcmin<sup>2</sup>. North is upward and east is to the left.

paper with the fluxes observed by Belley & Roy (1992); Kennicutt & Hodge (1980). The data are not corrected for interstellar reddening.

For the absolute calibration of *GALEX* data, we used zero point levels for *FUV* and *NUV* images (Morrissey et al. 2005).

We corrected all data for Galactic absorption; these values are indicated by an "0" subscript. We used the resulting ratio of the extinction in the *GALEX* bands to the color excess  $E(B - V)$  are  $A_{FUV}/E(B - V) = 8.24$  and  $A_{NUV}/E(B - V) = 8.2$  (Wyder et al. 2007).

### 3 SPIRAL ARMS

#### 3.1 Parameters of spiral arms

We investigate properties of spiral arms by curve fitting of two principal arms, which are clearly outlined in blue (*FUV*, *NUV*, *U*, *B*) passbands and  $H\alpha$  line (Fig. 1). The arms are defined by by-eye selection of pixels in the part of these images that is within the spiral arms. Pixels in this region are then fitted with a logarithmic spiral using linear least-squares.

A logarithmic spiral with a pitch angle  $\mu$  can be described as

$$r = r_0 e^{k(\theta - \theta_0)}, \quad (1)$$

where  $k = \tan \mu$ . We adopt two constraints for the fitting: the pitch angle is constant along the arm, and both spiral arms are symmetric.

We do not transform images of NGC 628 to the face-on position,  $i = 0^\circ$ , because the position of any point in the galaxy is changed by value much less than the characteristic width of the spiral arm, if we use the adopted inclination  $i = 7^\circ$ . Difference between the uncorrected position and the position corrected for the inclination position angle is less than  $0.5^\circ$  and the galactocentric distance  $\Delta r/r < 0.01$  for any point in the galaxy.

Spiral arm with a regular string of complexes found by Elmegreen & Elmegreen (1983) was named Arm A, and the opposite arm was named Arm B (Fig. 3). Arm A is known as Arm 2

in Kennicutt & Hodge (1976); Cornett et al. (1994) or South arm in Rosales-Ortega et al. (2011).

As a result of the fitting, we obtained coefficients in Eq. (1)  $r_0 = 21.95$  arcsec (765 pc) and  $k = 0.280$ , that corresponds to a pitch angle  $\mu = 15.7^\circ$ , for the arms. Zero point angle  $\theta_0 = -40^\circ$  for Arm A and  $140^\circ$  for Arm B (where  $\theta$  is counted from north toward east). The resulting spiral arms are shown in Fig. 3. Obtained pitch angle,  $\mu = 15.7^\circ$ , is close to the result of Kennicutt & Hodge (1976) who fitted every arm separately and obtained values  $13.8^\circ$  for Arm A and  $11.2^\circ$  for Arm B.

#### 3.2 Along-arm photometry

To study variation of brightness along a spiral arm, we obtained photometric profiles along Arms A and B. The elliptical aperture ( $40 \times 6$  arcsec<sup>2</sup>) with a minor axis along a spiral arm (i.e. a difference between P.A. of major axis and P.A. of the centre of aperture is a pitch angle), and a step of  $1^\circ$  by P.A. was used. Obtained photometric and colour indices profiles along the arms are presented in Fig. 4. For a logarithmic spiral in the form of Eq. (1), the longitudinal displacement along the spiral, denoted as  $s$ , is

$$s = (\sin \mu)^{-1} r_0 (e^{k(\theta - \theta_0)} - 1). \quad (2)$$

Star formation regions, visible in *FUV*, are absent in the innermost part of the spiral arms (Fig. 1). SFRs nearest to the galactic centre are located at distance  $r \approx 42 - 43$  arcsec in both arms. Therefore, we do not include the inner part of the spiral arms with a galactocentric distance  $r < 41.45$  arcsec (1.45 kpc) or an angular sector  $\theta - \theta_0 < 130^\circ$  in our research. Distorted outer part of Arm B was also excluded from the examination.

Using the profile in the *FUV* band, we have found local maxima of brightness on the profile. The local maxima of brightness were determined as lower extrema of the function  $m_{FUV}(s)$ . To locate them, we looked for points, where the first derivative of the function,  $dm(FUV)/ds = 0$  and  $d^2m(FUV)/ds^2 > 0$  on the profile (Fig. 5). Positions of these points also correspond to relatively bluer parts of spiral arms (Fig. 4).

We made only one exception when selecting local maxima of brightness. The additional maximum with the longitudinal displacement  $s = 13.7$  kpc in Arm A was included in the list of local maxima. The function  $dm(FUV)/ds$  does not attain 0 at this  $s$  (open circle in Fig. 5), however, obvious local maximum of brightness at  $s = 13.7$  kpc is observed on the profiles in the *U* band and  $H\alpha$  line (Fig. 4). The object which is responsible for this local maximum of brightness is a compact association, it is seen very well on the galactic images in the ultraviolet, *U* and  $H\alpha$  line (Figs. 1, 3, 6). It is shown by diamond in Fig. 6.

The maximum of brightness at the longitudinal displacement  $s = 7.5$  kpc in Arm A is a result of input from the bright interarm complex (Figs. 4, 5, 6); it was missed.

In a few cases, a shift of the maximum of brightness in different profiles along the longitudinal displacement  $s$  by 1 pixel is observed for the same objects; we adopt the position of the maximum on the *FUV* profile in such cases (see Figs. 4, 5).

Objects responsible for local maxima of brightness can be complexes, associations, star clusters and their groups. Strong maximum of the profile does not necessarily indicate the presence of a bright complex here. There may be somewhat independent associations or clusters, located at the same longitudinal displacement  $s$  along the arm. In addition, the radiation from bright SFRs can inhibit the radiation from fainter SFRs closely spaced along the arm. This is especially critical for profiles in the *FUV*. Therefore,

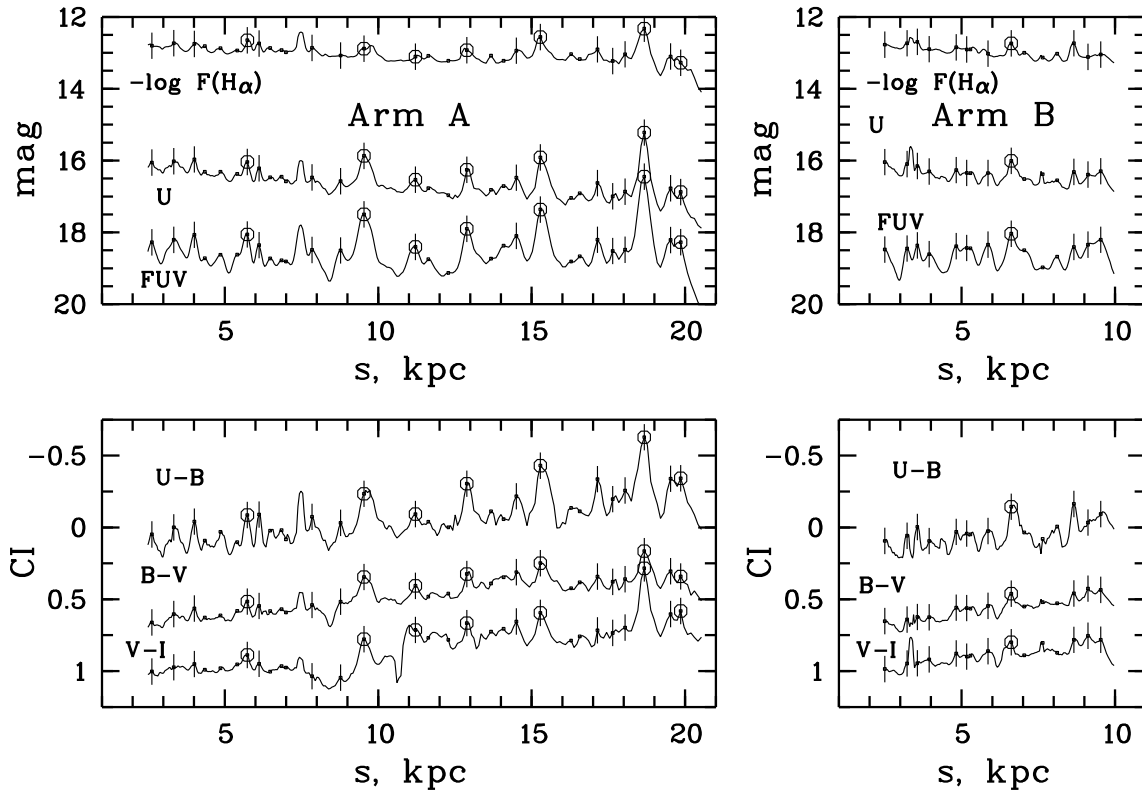


**Figure 4.** Photometric (top panels) and colour indices (bottom panels) profiles along Arm A (left panels) and Arm B (right panels). The units on the ordinate axis are corrected for Galactic absorption magnitudes, logarithm of  $H\alpha$  flux, and colour indices within the aperture. Positions of local maxima of brightness (dots), star formation regions (vertical bars) and bright complexes (circles) are indicated.

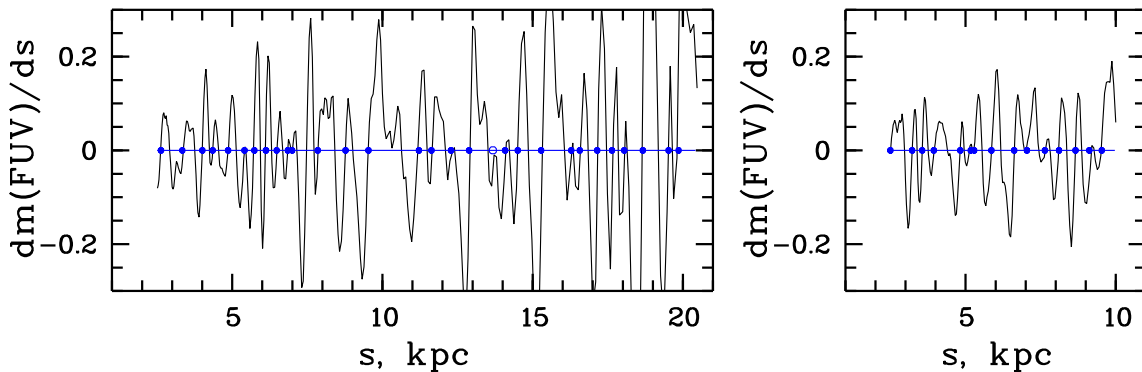


**Figure 5.** Function  $dm(FUV)/ds$  along Arm A (left panel) and Arm B (right panel). The circles indicate local maxima of brightness. See the text for more explanation.

to find and select bright star formation regions and complexes, we measured magnitudes of all objects in the arms of NGC 628 responsible for the local maxima of brightness on the profiles.

The photometry was made in round apertures, and the light from the surrounding background was subtracted from the light coming from the area, occupied by the star formation region. The technique of star formation regions photometry is described in more detail in Gusev & Park (2003); Bruevich et al. (2007).

As a result, we selected 30 star formation regions having a total magnitude  $FUV_0 < 19.7$  mag (Fig. 6). Follow-

ing Elmegreen & Elmegreen (1983), we divided the objects into bright complexes and fainter SFRs. Eight complexes brighter than 18.1 mag in  $FUV$  were selected as "bright complexes", other 22 objects were named "star formation regions". Unfortunately, we could not use "true" brightnesses, corrected for interstellar absorption, because extinction data, obtained from spectroscopic and spectrophotometric observations, are known not for all objects. We plan to study photometric properties, chemical abundances, sizes and estimation of ages of brightest star formation regions in Arms A and B in the further paper.

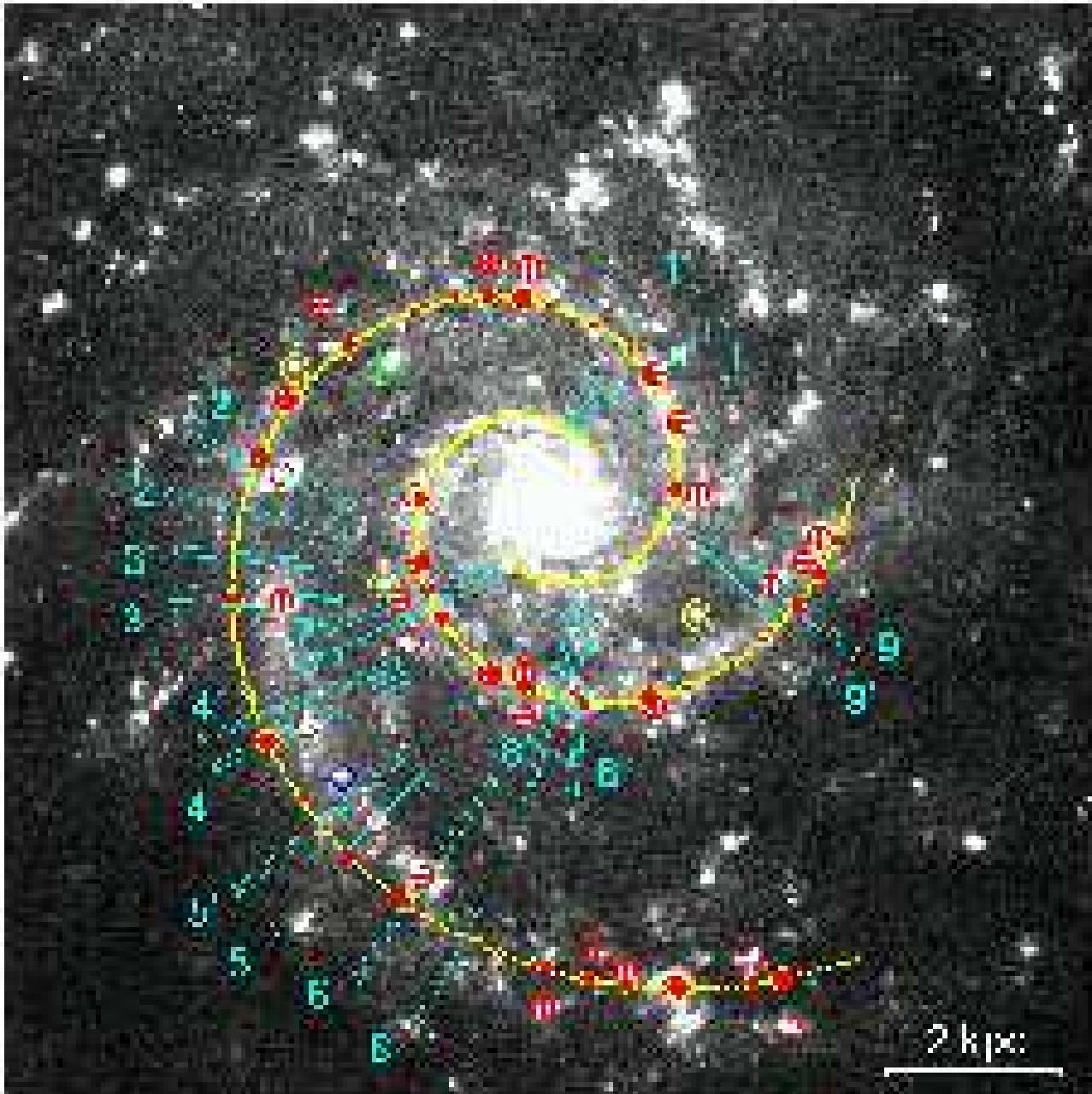


**Figure 6.** Image of NGC 628 in the  $U$  passband. Spiral arms are shown. The dark (red) large, middle and small circles on the arm's curves correspond to the projective positions of the bright complexes, star formation regions and the local maxima of brightness, respectively. The dark (red) crosses in circles show positions of the selected SFRs and complexes. The positions of across-arm profiles 1, 1'-9, 9' are indicated. The grey (green) square shows the interarm complex. The white (yellow) circles show the field stars, which have been removed from images before the along-arm photometry. The dark (blue) diamond shows the position of the additional association. The size of the image is  $6.0 \times 6.0$  arcmin<sup>2</sup>. North is upward and east is to the left. See the text for more explanation. (A colour version of this figure is available in the online version.) **High resolution jpeg image is available in the source format.**

The choice of lower limit of magnitude for bright complexes and star formation regions was subjective. We cut the list of bright complexes on the seventh brightest complex in Arm A; it coincides with the bright H II regions list of Elmegreen & Elmegreen (1983) with one exception (Figs. 1, 6). Among the regions fainter 19.7 mag in  $FUV$ , we found a large number of diffuse objects without a strong H $\alpha$  emission. Obviously, these regions are not complexes as determined in Efremov (1979, 1995). We will show below, that the variation of the limits of brightness does not affect our conclusion on principle.

We measured separations,  $l$ , between adjacent bright complexes, SFRs, and local maxima of brightness along each arm (Fig. 7). The set of the local maxima of brightness includes complexes and SFRs; the set of star formation regions includes bright complexes. Separation  $l$  between  $(n-1)^{st}$  and  $n^{th}$  regions is defined as  $s_n - s_{n-1}$ , where  $s \equiv s_n$  is defined from Eq. (2). Distribution of the regions by separation  $l$  in Arms A and B is presented in Fig. 8.

As seen from the figures, the regularity in spacing of both the SFRs and the local maxima of brightness is observed in spiral arms of the galaxy. The local maxima of brightness and the star forma-

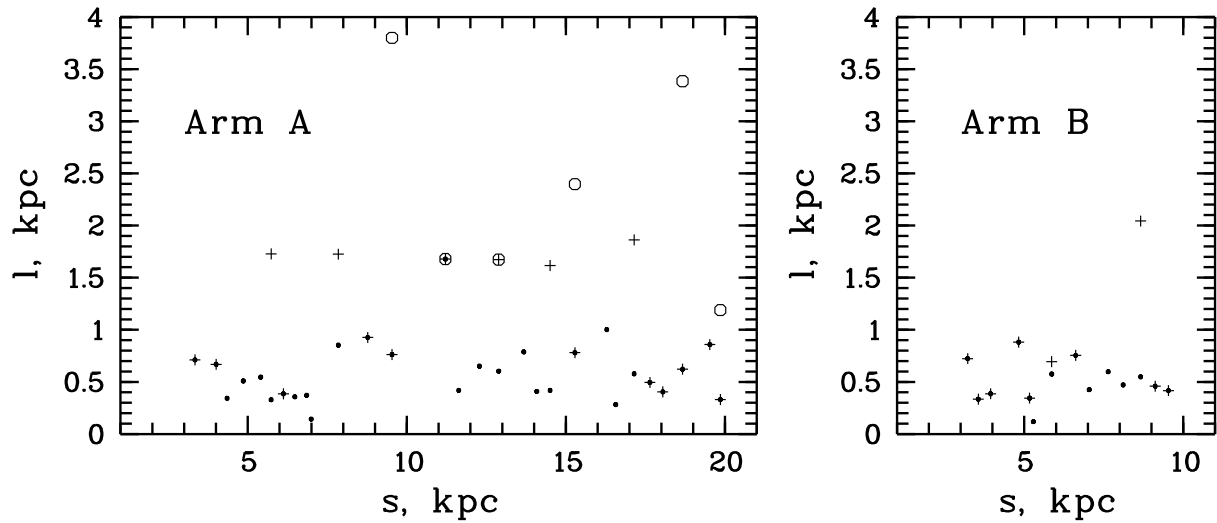


**Figure 7.** Separations  $l$  between adjacent local maxima of brightness (dots), star formation regions (crosses), and bright complexes (circles) along Arm A (left panel) and Arm B (right panel). See the text for more explanation.

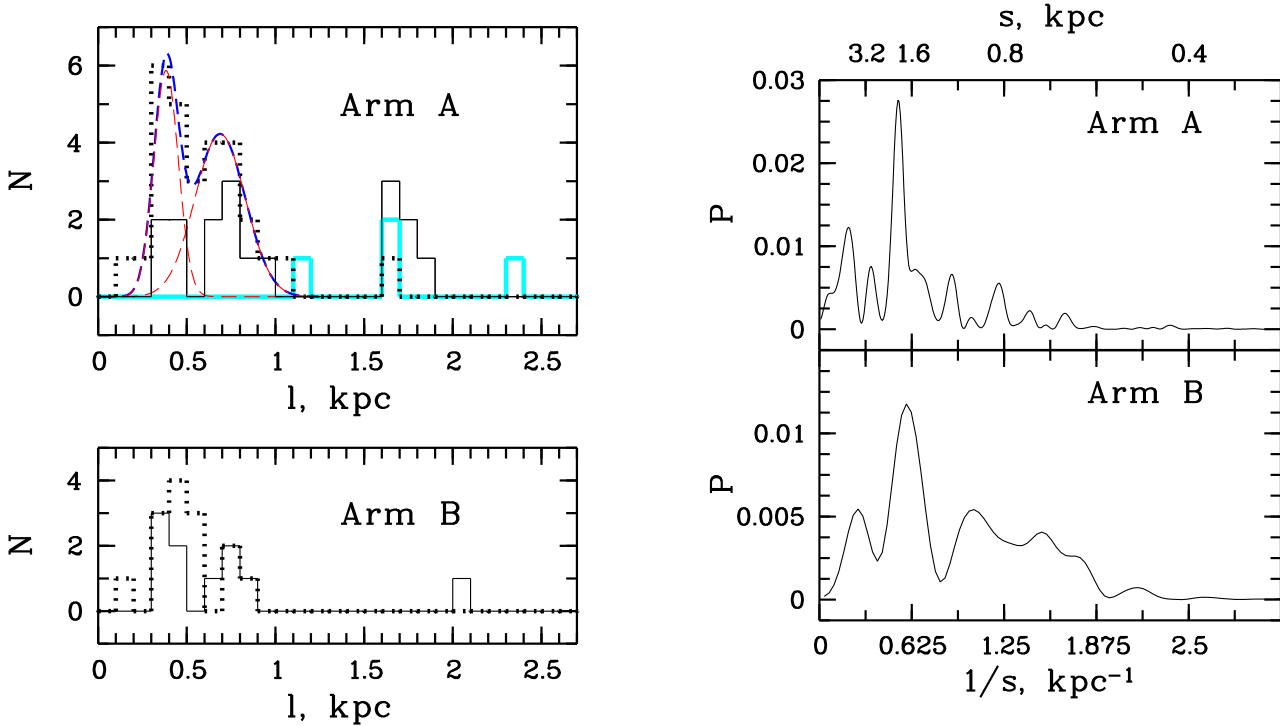


**Figure 8.** Number distribution histograms of the local maxima of brightness (thick dotted line), star formation regions (thick grey (cyan) solid line), and bright complexes (thin black solid line) by separation between adjacent objects along Arm A (top panel) and Arm B (bottom panel). The best fit Gaussians (grey (red) dashed lines) and their sum (thick dark (blue) dashed line) for the distribution of the local maxima of brightness in Arm A are shown.

**Figure 9.** Power spectra of the  $FUV$  profile data from Fig. 4 for Arm A (top panel) and Arm B (bottom panel).

tion regions show a multimodal distribution of distances between adjacent objects in both spiral arms (Fig. 8). We found a characteristic separation  $\Lambda \approx 400$  pc for the local maxima of brightness in both Arms A and B (Figs. 7, 8). This value is the same in inner part ( $s < 10$  kpc) of Arm A, where bright complexes are absent, and

in outer part of the arm, which is populated by bright complexes (Fig. 7). The distribution of the local maxima of brightness by separation has two maxima,  $\Lambda$  and  $2\Lambda$ , in both arms (Fig. 8). There are three characteristic separations ( $\Lambda$ ,  $2\Lambda$  and  $4\Lambda$ ) in Arm A and two ones ( $\Lambda$  and  $2\Lambda$ ) in Arm B are distinguished for the star formation regions. The characteristic separations of the bright complexes in Arm A is also multiple of  $\Lambda$  (Fig. 8).

For additional analysis, we estimated mean and median separations between local maxima of brightness and the star formation

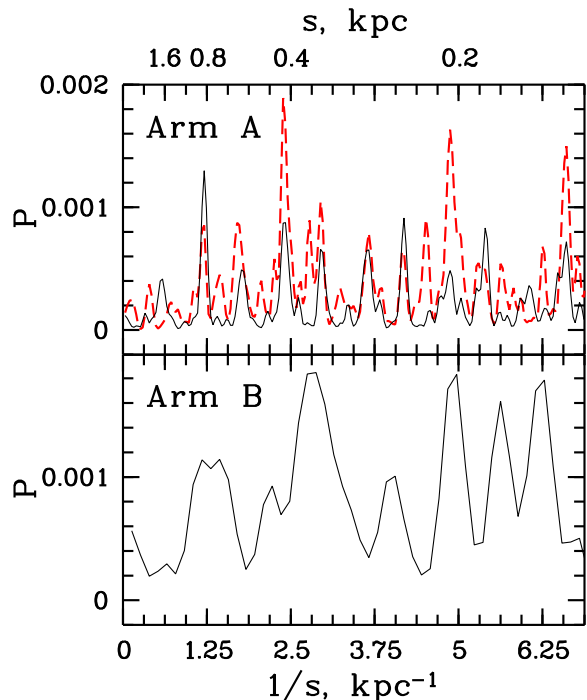


**Figure 10.** Power spectra of the function  $D(s)$  for local maxima of brightness (dark red dashed line) and star formation regions (black solid line) in Arm A (top panel), and star formation regions in Arm B (bottom panel).

regions in Arms A and B for individual subsets of the objects. Results are presented in Table 2.

The local maxima of brightness in Arm A at separations  $l < 1$  kpc can not be divided into two subsets visually on the histogram. We fitted the distribution of the local maxima of brightness of Arm A at  $l = 0.2 - 1.0$  kpc (26 points) using two Gaussians. The parameters of obtained Gaussians (mean values and standard deviations) are presented in Table 2. The profiles of two Gaussians and their sum are also shown in Fig. 8.

As seen from Table 2, the characteristic mean separations (i) are approximately equal to or multiple of  $\sim 0.4$  kpc, and (ii) they are close to each other in Arm A and Arm B.

Additionally, we calculated the power spectrum for the *FUV* magnitude data shown in Fig. 4 to estimate spacing regularity of star formation regions in Arms A and B (Fig. 9). Obtained power spectrum for the magnitude curve in Arm A has a basic peak at  $s \approx 2$  kpc. Secondary peaks at shorter wavelengths are observed at  $s \approx 1.6, 1.2,$  and  $0.8$  kpc (Fig. 9). Power spectrum for Arm B has a main peak at  $s \approx 1.6 - 1.7$  kpc and a secondary peak at  $s \approx 0.9 - 1.0$  kpc.

To find regularity in spacing of young stellar objects on the shorter wavelengths, we calculated the Fourier transform of the function  $D(s)$ , where  $D(s) = 1$  in points of the local maximum of brightness (star formation region) and  $D(s) = 0$  in all other points. Obtained power spectra of the function  $D(s)$  for the local maxima of brightness and star formation regions in Arm A, and the star formation regions in Arm B are presented in Fig. 10.

Results of the Fourier analysis qualitatively support the estimation of characteristic separations of local maxima of brightness and SFRs in the arms based on their distribution in Fig. 8. Power spectrum has strong peaks at  $s \approx 0.2$  and  $0.4$  kpc and weak peaks at  $s \approx 0.6$  and  $0.8$  kpc for the local maxima of brightness in Arm A; strong peaks at  $s \approx 0.4$  and  $0.8$  kpc and weak peaks at  $s \approx 0.6$  and

**Table 2.** Characteristic separations of the local maxima of brightness and the star formation regions in Arms A and B.

Sample	Arm A		Arm B	
	mean (kpc)	median (kpc)	mean (kpc)	median (kpc)
Local maxima of brightness	$0.38 \pm 0.07$	0.37	$0.46 \pm 0.09$	0.43
Star formation regions	$0.40 \pm 0.07$	0.39	$0.39 \pm 0.05$	0.35
	$0.76 \pm 0.11$	0.71	$0.76 \pm 0.08$	0.72
	$1.71 \pm 0.08$	1.68		

1.6 kpc for the SFRs in Arm A. Spectrum profile of SFRs in Arm B is smoother than profiles of the spectra for the objects in Arm A, nevertheless, peaks at  $s \approx 0.2, 0.4,$  and  $0.8$  kpc stand out (Fig. 10).

Based on data in Table 2, and assuming that separations between local maxima of brightness and SFRs are approximately equal to or multiple of  $\sim 0.4$  kpc, we obtained equations of the regular disposition of local maxima of brightness along Arms A and B of the galaxy:

$$s_m = 0.419s + 2.800 \quad (3)$$

for the local maxima of brightness in Arm A and

$$s_m = 0.391s + 2.421 \quad (4)$$

for objects in Arm B. Here,  $s_m$  is a position of local maximum of brightness (star formation region) along the spiral arm, and coefficients  $\Lambda = 0.419, 0.391$  kpc are the characteristic separations between local maxima of brightness and SFRs along Arm A and Arm B, respectively.

Using values  $s_m$  from Eqs. (3) and (4), we calculated deviations of actual positions of the local maxima of brightness along the spiral arm  $s$  from the nearest ones with positions  $s_m$  (Fig. 11). The figure shows a good spacing regularity of star formation regions in the greater part of Arm A. Average deviation  $s - s_m$  for SFRs located on longitudinal displacement  $s$  from 4 to 16 kpc is  $9 \pm 54$  pc (Fig. 11). In the outer part ( $s > 16$  kpc), Arm A widens, star formation regions are located both on the outer and the inner edge of the arm (Fig. 6). Disposition of star formation regions here is more poorly described by Eq. (3) than for the central part of Arm A. We observe that a chain of SFRs at  $s = 17 - 18$  kpc is displaced by  $\Lambda/2 \approx 0.2$  kpc relative to other SFRs (Fig. 11). Deviation of positions of star formation regions in Arm B from the positions  $s_m$  does not exceed 100 pc; an average deviation  $s - s_m = -11 \pm 62$  pc (Fig. 11).

Positions of local maxima of brightness in both spiral arms are slightly worse described by Eqs. (3) and (4) than positions of the SFRs (Fig. 11). Their average deviations  $s - s_m = 0 \pm 93$  pc ( $\pm 2\Lambda/9$ ) in Arm A and  $0 \pm 88$  pc ( $\pm 2\Lambda/9$ ) in Arm B. Thus, positions of most local maxima of brightness and star formation regions in both arms well satisfy the positions  $s_m$ , obtained from Eqs. (3) and (4).

Different used techniques complement each other to support presence of the regularity in spacing of SFRs in spiral arms of NGC 628. Power spectrum for the ultraviolet magnitude curve shows a periodicity at  $s \approx 1.6 - 2.0$  kpc ( $4\Lambda - 5\Lambda$ ) in both spiral arms (Fig. 9). Power spectrum of the function  $D(s)$  shows clear peaks at  $s \approx 0.4$  and  $0.8$  kpc ( $\Lambda$  and  $2\Lambda$ ) for the objects in both spiral arms (Fig. 10). Study of disposition of local maxima of brightness shows that the spacing regularity is observed throughout the parts of the spiral arms under study (one–two dozens of  $\Lambda$ ; Fig. 11). We

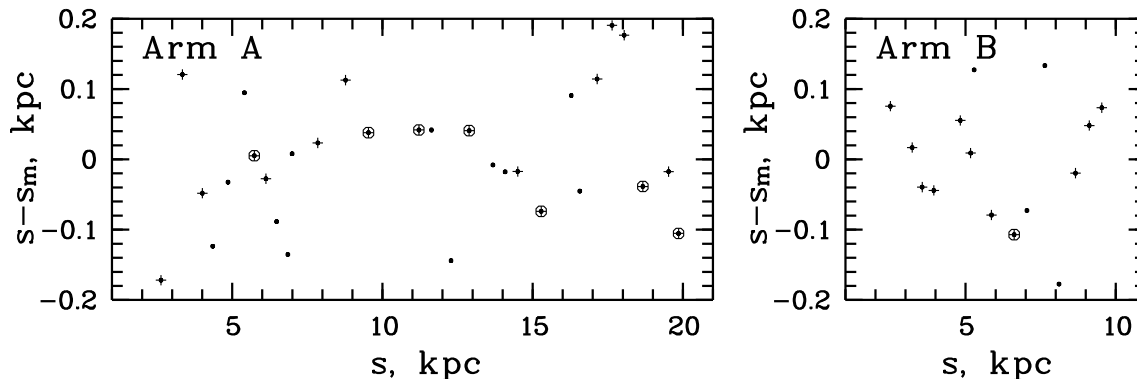


**Figure 11.** Deviations  $s - s_m$  for the local maxima of brightness (dots), star formation regions (crosses), and bright complexes (circles) along Arm A (left panel) and Arm B (right panel). See the text for more explanation.

suggest that the spacing regularity of local maxima of brightness and SFRs exists in both spiral arms of NGC 628 with a characteristic separation  $\Lambda \approx 400$  pc. Brighter regions have larger characteristic separations (Fig. 10 (top panel) illustrates it very well). The characteristic separation between adjacent bright complexes  $l = 4\Lambda \approx 1.6 - 1.7$  kpc corresponds to the estimation of the spacing  $L$ , which was found by Elmegreen & Elmegreen (1983) for their “H II regions” in Arm A of NGC 628.

However, the separations discussed above were measured along the arms. And for the smallest SFRs and especially for “the local maxima of brightness”, these separations are not distances between adjacent regions. We will return to that issue in Conclusion.

#### 4 DISCUSSION

Anticorrelation between shock wave signatures and the presence of star complexes chains is suspected in spiral arms of a few galaxies. The most evident is the M 31 case, where the regular chain of complexes (noted best in the *GALEX* images) is seen along the NW arm, whereas the stellar age gradient across the arm (well established with the Cepheid periods) and signatures of the shock wave are observed in another (S4, SW) arm, which structure is well described by the classical density wave theory (Efremov 2010).

The regular wave-like magnetic field is known just in the NW arm (Beck et al. 1989); therefore the magneto-gravitational instability might lead to formation of star complexes chain along this arm segment. Anticorrelation between the shock wave signature and regular spacing of complexes observed in M 31 may be explained with results of Dobbs & Price (2008), who concluded that spiral shocks generate an irregular magnetic field.

Amongst nearby galaxies, the most evident (after M 31) case of the above-mentioned anticorrelation is NGC 628 (M 74) galaxy. Unfortunately, there are no appropriate magnetic field data for the studied part of NGC 628. The only data concerning the magnetic field were obtained by Heald, Braun & Edmonds (2009) who detected polarized emission at 18 and 22 cm wavelengths from the outer part of the galaxy; their linear beam size was  $1.9 \times 0.5$  kpc.

Nevertheless, we can estimate some properties of interstellar medium based on the dust distribution in NGC 628. The dust lane along the stellar arm (but outside it) can be a signature of the spiral shock wave. In the case of NGC 628, we observe the dust lane running in front of inner edge of Arm B. It is clearly seen in the *U*

images of the galaxy (Figs. 1, 6), but farther from the center there is no dust lane running upstream of the stellar Arm A inner edge.

To study the disposition of the dust lanes along the spiral arms and variation of photometric parameters across the arms, we obtained photometric profiles across Arms A and B. Here, in addition to the ultraviolet and optical images, we used  $24 \mu\text{m}$  *Spitzer* (*MIPS*) image of the galaxy, taken from the *NED* database<sup>3</sup> (Dale et al. 2009), as a good tracer of dust location.

Nine positions for the cross-arm photometry were selected, six in Arm A, and three in Arm B (Fig. 6). Two profiles were obtained for each position; the first profile crosses the star formation region, and the second profile crosses the arm in the immediate vicinity of a SFR. The last set of profiles is marked as 1’-9’ (Fig. 6).

The length of across-arm profiles is from 55 to 80 arcsec, the width is equal to 3 arcsec for every profile. The fluxes across the P.A. of profile were averaged. Obtained profiles 1, 1’-9, 9’ of *FUV*<sub>0</sub> surface brightness and  $(U - B)_0$  colour index, and profiles 1’-9’ of  $24 \mu\text{m}$  flux are shown in Fig. 12. The marks  $r = 0$  arcsec correspond to positions of the logarithmic spiral in Fig. 6.

Photometric profiles in Fig. 12 clearly illustrate the hypothesis of Efremov (2010). Inside Arm B, the strong dust lane is located in the profiles 7, 7’ and 8, 8’ at  $r \approx +10$  arcsec. Ultraviolet surface brightness goes down there to  $\approx 25.5$  mag arcsec<sup>-2</sup>, colour index  $U - B$  increases to  $\approx 0.5$  mag, and  $24 \mu\text{m}$  flux reaches a maximum (Fig. 12). Smoothed dust lane is also observed in the profiles 9, 9’ at  $r \approx +10 - +20$  arcsec. Note that further along Arm B, in its distorted outer part, several large complexes are observed (Fig. 6). These complexes are brighter than the regions in the studied inner part of Arm B.

Visually in optical images Arm A does not show obvious traces of dust lane, at least in its outer part (Fig. 1). However, the increase of the colour index  $U - B$  at  $r = +5$  arcsec in profile 1’,  $r = -11$  arcsec in profiles 2’, 5’ and 6’, and  $r = -15$  arcsec in profile 4’ is in accordance with the position of the dust lane inside the stellar Arm A. Maxima of  $24 \mu\text{m}$  flux in profiles 2’-5’ are also consistent with the middle of the stellar arm (Fig. 12).

As Fig. 13 demonstrates, the 2.6 mm ( $\text{CO}/\text{H}_2$ ) profiles across spiral arms repeat ultraviolet profiles with a few exceptions. In the beginning of the Elmegreens’ chain of complexes (profiles 2, 2’ and 3, 3’), the maximum of the CO flux shifts to the centre with respect to the *FUV* maximum. Fig. 13 shows that the CO lane is

<sup>3</sup> <http://ned.ipac.caltech.edu/>

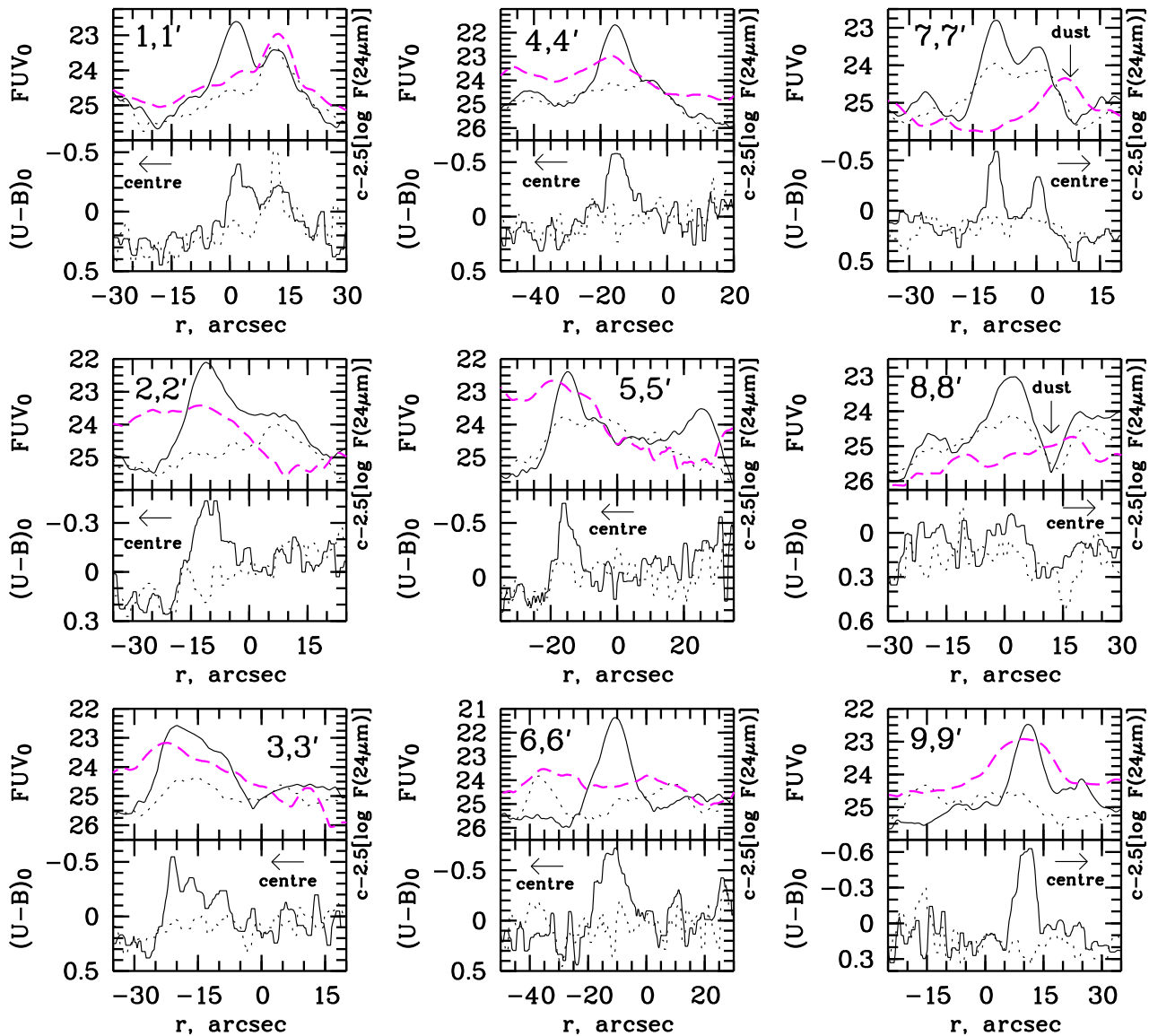


**Figure 12.**  $FUV_0$  photometric,  $(U - B)_0$  colour index (black lines), and  $24 \mu\text{m}$  (dark (magenta) lines) profiles across Arm A (left and central panels) and Arm B (right panels). Positions of profiles 1, 1'–9, 9' are shown in Fig. 6. Solid lines correspond to profiles 1–9, dotted and dashed lines correspond to profiles 1'–9'.  $C$  is an arbitrary constant for scaling the  $24 \mu\text{m}$  curves. Directions to the galactic centre and positions of dust lanes indicated by arrows. See the text for more explanation.

rather located along the inner side of stellar arms (see profiles 1, 1', 4, 4', 5, 5', 7, 7').

The overall comparative morphology of spiral arms in NGC 628 is demonstrated in Fig. 14 for the different wave lengths. One may see that the CO ( $2.6 \text{ mm}$ ,  $\text{CO}/\text{H}_2$ ) lanes go along the inner sides of both stellar arms, but further on along Arm A, the dust lane goes inside this arm and about here the regular spacing of stellar complexes along Arm A appeared (Fig. 14). No such a regularity is seen in Arm B, and there is no regular spacing of star complexes as well.

One might think the strong dust lane along the inner side of the stellar Arm B is seen in optics so evidently only due to its bright stellar background, but Fig. 14 demonstrates it is not so – the  $\text{CO}/\text{H}_2$  lane along the inner side of Arm B is seen very well, whereas it absents along the arm outer side. As concerns Arm A,

the age gradient (shift between CO and UV arms) is observed to the same distance from the center, at which Arm B becoming quite irregular (Fig. 14). Comparison of  $NUV$ , CO, and  $8 \mu\text{m}$  images in Fig. 14 demonstrates, that further from the center in Arm A, the  $8 \mu\text{m}$  and stellar arm central lines coincide.

This is exactly the same situation as observed in the NW segment of M 31 spiral arm, where star complexes are seen inside the dust/gas lane. There was a suspicion that this M 31 situation might be due to the local plane corrugation which might present us the gas lane projected onto the stellar arm (whereas the former might be in fact closer to the galaxy center in the M 31 plane). Face-on orientation of the M 74 plane makes such an explanation untenable.

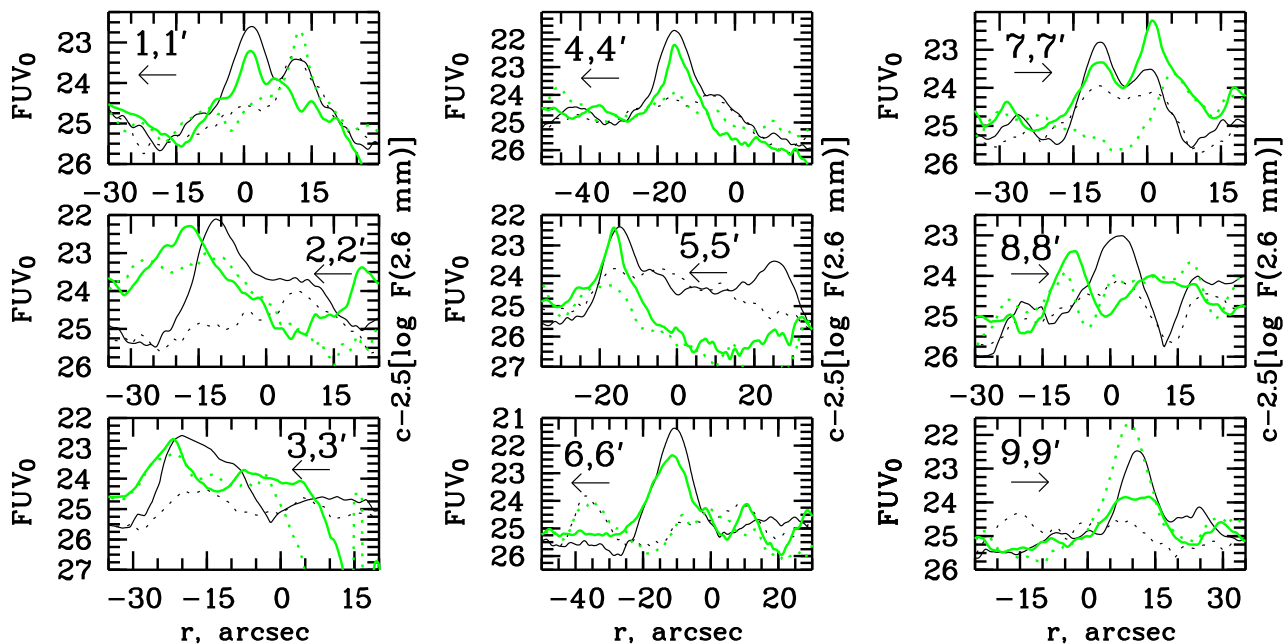


**Figure 13.**  $FUV_0$  photometric and 2.6 mm flux (CO; grey (green) lines) profiles across Arm A (left and central panels) and Arm B (right panels). Solid lines correspond to profiles 1–9, dotted lines correspond to profiles 1'–9'.  $C$  is an arbitrary constant for scaling the CO curves. Directions to the galactic centre indicated by arrows.

## 5 CONCLUSIONS

Our results confirms the drastic difference in the inner structures between the spiral arms of NGC 628, one of which is long and hosts the regular chain of star complexes and another does not. Elmegreen & Elmegreen (1983) in the first study of star complexes strings in the spiral arms found altogether 22 galaxies with such strings, and only in 7 of these the chains were noted along both arms; the NGC 628 case seems to be typical. The reasons for such a difference are unknown yet. Moreover, it is unclear until now why only some 10% of galaxies (all of the grand design type) searched by these authors for complexes chains were found to host such chains.

This statistics should be enlarged, but one might suggest already that indeed the magneto-gravitational instability – and not just the gravitational only – should be involved in string of complexes formation. Magnetic field – and more so regular field along an arm – is surely more rare phenomenon as comparing with the universal law of gravitation. If so, occurrence of the regular chain in the minority of stringed arms only may imply we do not know yet some essential properties of intergalactic magnetic fields. The cause of drastic difference in inner structures of otherwise symmetric arms (in well isolated galaxies!) seems to be amongst the greatest unsolved issues in understanding the spiral structures of galaxies.

Another our result (which is to be confirmed still) may imply existence of a certain minimal distance between young star groups, measured in projection onto the arm central line. Many of these groups are too small to be called "a complex", but most distances are either this minimal one (about 400 pc, assuming the galaxy distance is 7.2 Mpc – probably it is larger) or twice and four times this minimal distance. This distance is seen well within Arm A between complexes A3 and A6. We cannot exclude the possibility that in-

cluding of associations from Arm B, which distributed there rather chaotically – and not along the arm – may lead to erroneous (too short) estimate of this "fundamental" length.

However, the physical sense of these preferred distances becomes uncertain in the central region of the galaxy and this concerns both the arms. In this region distances between SFRs, projected onto the central lines of both arms cannot be considered as the distance along the arm. This issue should be considered in more details. It is quite probable that this central region should be excluded from the consideration of the characteristic distances between SFRs.

At any rate, we see that both arms of M 74 galaxy are quite different (though are symmetrical in relation to the galaxy center). The longer Arm A contains the chain of star complexes, whereas the shorter Arm B hosts the (irregular) chains of (rather small) H II regions as well as dust lanes, one quite strong along the inner side of the stellar arm and another lane, much lesser expressed along the outer side. Implications of the later phenomena should be studied yet.

The last unsolved issue we want to mention here is missing of a complex (i.e. the double distance between adjacent complexes) in a string, which was noted already in Elmegreen & Elmegreen (1983). They found that some of their "H II regions" have double mutual distance as comparing with the average expected between two ones along a given arm. Similarly, later Efremov (2010) found that some distances between regularly spaced H I superclouds along the Carina arm of the Galaxy are twice larger than all others. These facts are hardly possible to explain in other way apart from the gravitational or, rather, magneto-gravitational instability, developing along the arm in the gas tube to form superclouds, the parent bodies for star complexes. Unfortunately, the HST data are not available for the outer part of Arm A, where the regular chain of complexes is observed.

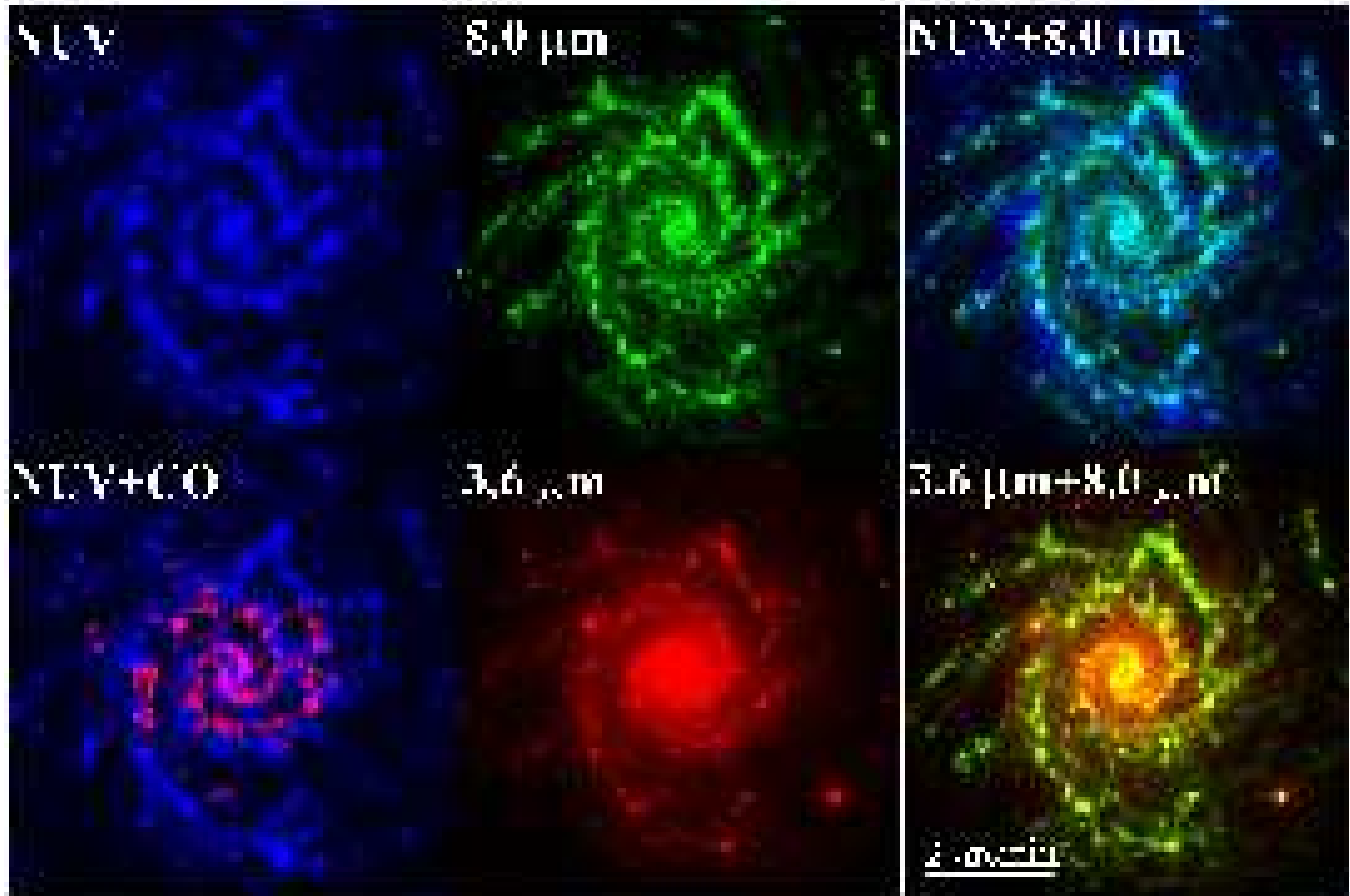


**Figure 14.** The morphology of the NGC 628 spiral structure. The composition of the fits images, taken from the NED (<http://ned.ipac.caltech.edu>; Dale et al. 2009; Regan et al. 2001; Helfer et al. 2003): *GALEX* Near UV image (indicator of young stars), *Spitzer* (IRAC) 8.0  $\mu\text{m}$  image (indicator of dust and PAH molecules), *Spitzer* (IRAC) 3.6  $\mu\text{m}$  image (indicator of old red giants), *NRAO* 2.6 mm (CO) image (indicator of  $\text{H}_2$ ), and their overlay. (A colour version of this figure is available in the online version.) **High resolution jpeg image is available in the source format.**

## ACKNOWLEDGMENTS

We are grateful to the referee for his/her constructive comments. The authors would like to thank E. V. Shimanovskaya (SAI MSU) for help with editing this paper. The authors acknowledge the usage of the HyperLeda data base (<http://leda.univ-lyon1.fr>), Barbara A. Miculski archive for space telescopes (<http://galex.stsci.edu>) and the NASA/IPAC Extragalactic Database (<http://ned.ipac.caltech.edu>). This study was supported in part by the Russian Foundation for Basic Research (project no. 12-02-00827).

## REFERENCES

- Artamonov B. P. et al., 2010, *Astron. Rep.*, 54, 1019  
 Banse K., Crane Ph., Ounnas Ch., Ponz D., 1983, MIDAS, in Proc. of DECUS, Zurich, p. 87  
 Beck R., Loiseau N., Hummel E., Berkhuijsen E. M., Grave R., Wielebinski, R., 1989, *A&A*, 222, 58  
 Belley J., Roy J.-R., 1992, *ApJS*, 78, 61  
 Bruevich V. V., Gusev A. S., Ezhkova O. V., Sakhibov F. Kh., Smirnov M. A., 2007, *Astron. Rep.*, 51, 222  
 Cornett R. H. et al., 1994, *ApJ*, 426, 553  
 Dale D. A. et al., 2009, *ApJ*, 703, 517  
 de la Fuente Marcos R., de la Fuente Marcos C., 2009, *ApJ*, 700, 436  
 Dobbs C. L., Price D. J., 2008, *MNRAS*, 383, 497  
 Efremov Yu. N., 1979, *Sov. Astron. Lett.*, 5, 12  
 Efremov Yu. N., 1989, *Sites of Star Formation in Galaxies: Star Complexes and Spiral Arms*. Fizmatlit, Moscow, p. 246 (in Russian)  
 Efremov Yu. N., 1995, *AJ*, 110, 2757  
 Efremov Yu. N., 2009, *Astron. Lett.*, 35, 507  
 Efremov Yu. N., 2010, *MNRAS*, 405, 1531  
 Efremov Yu. N., 2011, *Astron. Rep.*, 55, 108  
 Efremov Yu. N., Elmegreen B. G., 1998, *MNRAS*, 299, 588  
 Elmegreen B. G., 1994, *ApJ*, 433, 39  
 Elmegreen B. G., 2009, in Andersen J., Bland-Hawthorn J., Nordström B., eds, *Proc. IAU Symp. 254, The Galaxy Disk in Cosmological Context*. Kluwer, Dordrecht, p. 289  
 Elmegreen B. G., Efremov Yu. N., 1996, *ApJ*, 466, 802  
 Elmegreen B. G., Elmegreen D. M., 1983, *MNRAS*, 203, 31  
 Grøsbøl P. J., Ponz J. D., 1990, *The MIDAS System*, in Longo G. and Sedmak G., eds, *Acquisition, Processing and Archiving of Astronomical Images*, OAC and FORMEZ, p. 109  
 Gusev A. S., Park M.-G., 2003, *A&A*, 410, 117  
 Heald G., Braun R., Edmonds R., 2009, *A&A*, 503, 409  
 Helfer T. T., Thornley M. D., Regan M. W., Wong T., Sheth K., Vogel S. N., Blitz L., Bock D. C.-J., 2003, *ApJS*, 145, 259

- Kennicutt R. C., Hodge P. W., 1976, *ApJ*, 207, 36  
Kennicutt R. C., Hodge P. W., 1980, *ApJ*, 241, 573  
Morrissey P. et al., 2005, *ApJ*, 619, L7  
Odekon M. C., 2008, *ApJ*, 681, 1248  
Paturel G., Petit C., Prugniel Ph., Theureau G., Rousseau J.,  
Brouty M., Dubois P., Cambresy L., 2003, *A&A*, 412, 45  
Regan M. W., Thornley M. D., Helfer T. T., Sheth K., Wong T.,  
Vogel S. N., Blitz L., Bock D. C.-J., 2001, *ApJ*, 561, 218  
Rosales-Ortega F. F., Diaz A. I., Kennicutt R. C., Sanchez S. F.,  
2011, *MNRAS*, 415, 2439  
Sakhibov F. Kh., Smirnov M. A., 2004, *Astron. Rep.* 48, 995  
Sharina M. E., Karachentsev I. D., Tikhonov N. A., 1996, *A&AS*,  
119, 499  
van Dyk S. D., Li W., Filippenko A. V., 2006, *PASP*, 118, 351  
Wyder T. K. et al., 2007, *ApJS*, 173, 293

This figure "MN-13-0186-MJ-Fig01.jpg" is available in "jpg" format from:

<http://arxiv.org/ps/1306.1731v1>

This figure "MN-13-0186-MJ-Fig06.jpg" is available in "jpg" format from:

<http://arxiv.org/ps/1306.1731v1>

This figure "MN-13-0186-MJ-Fig14.jpg" is available in "jpg" format from:

<http://arxiv.org/ps/1306.1731v1>